

Analysing the plausibility of iron-core white dwarfs

Ethan Tregidga 30731003¹*

¹*Faculty of Engineering and Physical Sciences, University of Southampton, Southampton SO17 1BJ, UK*

25 October 2022

ABSTRACT

This report aims to model the internal structure of white dwarf stars and identify if there is any evidence supporting the existence of iron white dwarf stars. The internal structure of a white dwarf star is determined by the electron degeneracy pressure, which two partial differential equations can model. The two equations can be solved using the numerical Runge-Kutta method to produce mass-radius and density-radius relationships for a white dwarf star. Several of these simulations are run to determine the radius and mass of a white dwarf over a range of different core densities. Finally, a stellar mass-radius plot was created to identify the relationship between a white dwarf’s mass and its radius. Data from two different surveys of white dwarfs was compared to the model of the different core types. The data generally agrees well with the models; however, there are some inaccuracies at the extremes of white dwarf masses. This report found that the carbon-oxygen model better fitted the more recent data than the iron-core model. Older data was found to agree more with the iron model; however, more recent measurements of the same white dwarf stars conformed better with the carbon-oxygen model. Therefore, this paper found no conclusive evidence for the existence of iron-core white dwarf stars.

Key words: White dwarfs – Runge-Kutta – Partial differentials – Iron-cores

1 INTRODUCTION

This paper aims to model the structure of a white dwarf composed of different nuclei to identify if existing data points towards the existence of iron-core white dwarfs.

A white dwarf star is a compact degenerate core of a star that has burned all available fuel. Typically, stars are in hydrostatic equilibrium where the fusion from the core provides an outward pressure counteracting the force of gravity. However, white dwarfs no longer have fusion in the core and require some other form of pressure to prevent their collapse.

A white dwarf is typically the result of the collapse of a low to intermediate-mass star in the range $0.07 M_{\odot} \leq M_* \leq 10 M_{\odot}$. $0.07 M_{\odot}$ is the lower limit for hydrogen burning in low metallicity stars (Chabrier & Baraffe 1997). $10 M_{\odot}$ is the upper limit for stable carbon burning (Heger et al. 2003) after which, the progenitor star will have enough mass to fuse up to iron, where it will form a different remnant star and undergo other supernovae fates. The mass of the star defines which nuclei the star can fuse. More massive stars can generate more significant pressures in the core, which allows the fusion of heavier elements. When the star can no longer fuse the products in the core, there will be no force counteracting gravity resulting in the collapse and then ejection of the outer layers of a star creating a planetary nebula with the core, now a white dwarf, at the center.

Main sequence stars with a mass in the range $0.07 M_{\odot} \leq M_* \leq 0.8 M_{\odot}$, will only burn hydrogen into helium, and the composition of

the remnant star will be a helium white dwarf. For stellar masses in the range $0.8 M_{\odot} \leq M_* \leq 8 M_{\odot}$, the star will be able to fuse helium into carbon and oxygen; however, it cannot fuse carbon; therefore, it will produce a carbon-oxygen white dwarf (Pols 2011). Finally, the last mass range that will produce a white dwarf is from $8 M_{\odot} \leq M_* \leq 10 M_{\odot}$ where the star can fuse carbon into neon and magnesium, but it is unable to produce any other heavier elements. These stars, depending on specific parameters, will either produce a neutron star or an oxygen-neon-magnesium white dwarf (Heger et al. 2003).

The core of a white dwarf is composed of nuclei and electrons and as there is no fusion to create an outwards pressure, white dwarfs are very dense, reaching maximum core densities in $kg m^{-3}$ of 12 orders of magnitude (Leung & Nomoto 2018). Electron degeneracy pressure is responsible for preventing the collapse of the remnant star. Electron degeneracy pressure comes from the fact that electrons are fermions and, therefore, have to obey Pauli’s exclusion principle, which states that only one fermion can occupy the same quantum state at the same time. Pauli’s exclusion principle, therefore, prevents the compression of electrons if this would result in their wavefunctions overlapping.

However, electron degeneracy pressure is not the absolute limit to the density of matter as there are two additional forms of matter that can reach greater densities. The first is neutron degeneracy pressure which occurs in neutron stars. Neutron degeneracy pressure is where the protons have captured all the electrons resulting in neutrons being the only particle in the core of a neutron star. As neutrons are fermions, they also have to obey Pauli’s exclusion principle, resulting in neutron degeneracy pressure.

Finally, black holes contain the last state of matter. Black holes are

* E-mail: et1g19@soton.ac.uk

where gravity has reached a point where not even neutron degeneracy pressure can prevent the collapse of a star. However, not much is known about the state of matter inside a black hole.

The point where the force of gravity can overpower electron degeneracy pressure by forcing electron capture is vital to understand, as this will create an upper limit to the mass of a white dwarf. The upper limit to the mass of a white dwarf is called the Chandrasekhar mass. It is given by equation 1 (Chandrasekhar 1984) where μ_e is the mean molecular weight per free electron, A_i is the atomic mass, Z_i is the atomic number, and X_i is the mass fraction for an atomic species (Pols 2011).

$$M_{lim} = 5.76\mu_e^{-2} M_{\odot}, \quad \mu_e = \sum_i \frac{A_i}{Z_i X_i} \quad (1)$$

Therefore, as helium, carbon, oxygen, neon and magnesium all have a ratio of $\frac{A}{Z} = 2$, so $\mu_e = 2$ and the theoretical Chandrasekhar mass for the three main types of white dwarfs would be $M_{lim} = 1.44 M_{\odot}$.

However, due to the discovery of several white dwarf stars with radii smaller than can be explained by previous models, iron-core white dwarfs were theorised to explain this discrepancy. The result of smaller radii suggests that the cores are made from nuclei of larger atomic masses with fewer electrons generating the outwards pressure.

If iron white dwarfs exist, then they would have a different value for the Chandrasekhar mass as iron has a ratio of $\frac{A}{Z} = 2.15$, therefore, $M_{lim} = 1.25 M_{\odot}$.

However, iron-core white dwarf stars are contentious as their formation cannot be easily explained. One possible formation process was discussed in two papers by Jordan et al. (2012), and Isern et al. (1991) where a type Ia supernova fails to unbind the white dwarf. The supernova explosion ejects a fraction of the white dwarf's mass with some energy converted to fuse nuclei into a mix of intermediate and iron group elements. This mass can then fall back onto the white dwarf, with the heavy elements migrating to the core of the white dwarf forming an iron-rich white dwarf. However, there has not been any conclusive evidence for this type of supernovae.

One of the first white dwarf stars to point towards the existence of iron white dwarfs was 40 Eridani B which over the years has had a variety of measurements for its mass from as low as $0.43 \pm 0.02 M_{\odot}$ from Heintz (1974). Due to the low mass of the white dwarf, it was suggested to be a helium white dwarf.

Later measurements by Provencal et al. (1998) provided an estimate of the radius to be $13.6 \pm 0.2 \cdot 10^{-3} R_{\odot}$. The small mass and radius would require a core made of iron; however, the paper also provided an updated mass estimate of $0.501 \pm 0.011 M_{\odot}$ which a carbon-oxygen core can now explain.

In a paper by Bond et al. (2017), the new mass and radius estimates were $0.573 \pm 0.018 M_{\odot}$ and $13.08 \pm 0.20 \cdot 10^{-3} R_{\odot}$, respectively, which now falls within the expected values for a carbon-oxygen white dwarf.

In a paper by Provencal et al. (1998), they used data from Hipparcos to calculate the mass and radius of several white dwarf stars. This data was then used by Panei et al. (1999), who concluded that there were three likely candidates for iron-core white dwarfs as they had significantly smaller radii for their masses. These stars were GD 140, EG 50 and Procyon B which had masses $0.79 \pm 0.02 M_{\odot}$, $0.50 \pm 0.02 M_{\odot}$ and $0.604 \pm 0.018 M_{\odot}$ and radii $8.5 \pm 0.5 \cdot 10^{-3} R_{\odot}$, $10.4 \pm 0.6 \cdot 10^{-3} R_{\odot}$ and $9.6 \pm 0.4 \cdot 10^{-3} R_{\odot}$, respectively.

Future calculations from Provencal et al. (2002) have since increased the radius of Procyon B to $12.34 \pm 0.32 \cdot 10^{-3} R_{\odot}$ which now places the remnant star within the uncertainty of the mass-radius relation for carbon-oxygen white dwarfs.

However, there have not been any updated numbers for GD 140 or EG 50, leaving them as potential iron white dwarf stars.

2 METHOD

The goal of modelling the structure of a white dwarf is first to find two first-order partial differential equations that link mass and density to the radius. These partial differential equations should be dimensionless to reduce errors due to extreme magnitudes in numbers.

The masses and densities can then be calculated for different radii by numerically solving these partial differential equations using the Runge-Kutta method.

Finally, the mass and radii of experimentally observed white dwarf stars can be plotted on a graph with the model to identify the model's accuracy and if there is enough evidence to suggest the existence of iron white dwarfs.

2.1 Derivation of differential equations

First, this model assumes that the star is spherically symmetric and that the star is not rotating and, therefore, there are no rotational forces. Additional assumptions are that the white dwarf is homologous, made of atoms with the same $\frac{A}{Z}$ ratio and that the white dwarf has no atmosphere.

The star has a total mass, M , and a radius, R .

Starting from a small packet of mass, Δm , at a radius, r , where $r < R$, then the force of gravity, F_g , acting on this packet of mass, is given by equation 2 where $m(r)$ is the enclosed mass.

$$F_g = \frac{-Gm(r)\Delta m}{r^2} \quad (2)$$

Assuming that the star is in hydrostatic equilibrium, then the force due to pressure, equation 3, must equal the force of gravity, where ρ is the density of the packet.

$$F_p = -\frac{1}{\rho} \frac{dP}{dr} \Delta m \quad (3)$$

Therefore, combining the two equations gives

$$\frac{dP}{dr} = -\frac{Gm(r)}{r^2} \rho(r) \quad (4)$$

Equation 4 can be rearranged to find $\frac{d\rho}{dr}$ using the chain rule; therefore, if an equation for $\frac{dP}{d\rho}$ is known, then the first partial differential can be calculated.

2.1.1 Pressure-density relationship

Assuming that the white dwarf is in a fully electron degenerate state so that the only source of pressure comes from electrons which have a momentum up to the Fermi momentum, p_F , the equation of state for pressure is given by

$$P = \frac{1}{3} \int_0^{\infty} n(p) p v dp \approx \frac{1}{3} \int_0^{p_F} n(p) p v dp \quad (5)$$

where $n(p)$ is the number density, p is the momentum, and the velocity, v , is given by

$$p^2 + m_e^2 c^2 = \frac{m_e^2 c^2}{1 - \frac{v^2}{c^2}}, \quad v = \frac{p/m_e}{\sqrt{1 + \left(\frac{p}{m_e c}\right)^2}} \quad (6)$$

where m_e is the mass of an electron.

The Fermi momentum can be calculated using Fermi-Dirac statistics where ϵ_p is the energy as a function of momentum, μ is the chemical potential, and T is the temperature.

In the degenerate limit, $\epsilon_p = \mu$, therefore,

$$n(p) = \frac{8\pi}{h^3} \frac{p^2}{\exp\left(\frac{\epsilon_p - \mu}{k_B T}\right) + 1} \approx \frac{8\pi}{h^3} p^2 \quad (7)$$

The number density, $n(p)$, can be integrated up to p_F and using $n = \frac{\rho}{\mu m_u}$, where μ is the mean mass in atomic units and m_u is the atomic mass,

$$n = \int_0^{p_F} n(p) dp = \frac{8\pi}{3h^3} p_F^3, \quad p_F = h \left(\frac{3}{8\pi \mu m_u} \right)^{\frac{1}{3}} \rho^{\frac{1}{3}} \quad (8)$$

Then, by using the chain rule, $dp = \frac{dp}{d\rho} d\rho$ and differentiating equation 5 with respect to ρ , you get

$$\frac{dP}{d\rho} = \frac{8\pi c}{3m_e h^3} p_F^4 \left(1 + \left(\frac{p_F}{m_e c} \right)^2 \right)^{-\frac{1}{2}} \left. \frac{dp}{d\rho} \right|_{p_F} \quad (9)$$

where $\left. \frac{dp}{d\rho} \right|_{p_F} = \frac{p_F}{3\rho}$ and using equation 8, then

$$\frac{dP}{d\rho} = \frac{h^2 \rho^{\frac{2}{3}}}{3\mu m_e m_u} \left(1 + \left(\frac{p_F}{m_e c} \right)^2 \right)^{-\frac{1}{2}} \quad (10)$$

Finally, using the assumption that the electrons are the only source of pressure, $\mu = \mu_e = Y_e^{-1}$, and using the substitution $\frac{p_F}{m_e c} = \left(\frac{\rho}{\rho_0} \right)^{\frac{1}{3}}$ where

$$\rho_0 = \frac{8\pi m_u m_e^3 c^3}{3Y_e h^3}, \quad (11)$$

then

$$\frac{dP}{d\rho} = Y_e \frac{m_e c^2}{m_u} \frac{\left(\frac{\rho}{\rho_0} \right)^{\frac{2}{3}}}{3 \left(1 + \left(\frac{\rho}{\rho_0} \right)^{\frac{2}{3}} \right)^{\frac{1}{2}}} = Y_e \frac{m_e c^2}{m_u} \gamma \left(\frac{\rho}{\rho_0} \right) \quad (12)$$

2.1.2 Density-radius relationship

The density partial differential equation can be calculated by using the chain rule, $\frac{d\rho}{dr} = \frac{d\rho}{dP} \frac{dP}{dr}$, therefore, using equations 4 and 12,

$$\frac{d\rho}{dr} = -\frac{Gm(r)}{Y_e r^2} \frac{m_u}{m_e c^2} \gamma \left(\frac{\rho}{\rho_0} \right)^{-1} \quad (13)$$

In order to solve this equation using the Runge-Kutta method, the equation must be made dimensionless. The following substitutions can be made

$$x = \frac{r}{R_0}, \quad y = \frac{\rho}{\rho_0}, \quad z = \frac{m}{M_0} \quad (14)$$

therefore, combining equations 13 and 14, you get

$$\frac{dy}{dx} = -\frac{yz}{x^2} \frac{M_0}{R_0} \frac{Gm_u}{Y_e m_e c^2 \gamma(y)} \quad (15)$$

and defining M_0 by

$$M_0 = \frac{4}{3} \pi \rho_0 R_0^3 \quad (16)$$

then, combining the equation for M_0 with equation 11,

$$\frac{dy}{dx} = -\frac{yz}{x^2 \gamma(y)} \frac{4Gm_u^2 m_e^2 c}{9\pi h^3 Y_e^2} R_0^2 \quad (17)$$

Therefore, if R_0 is defined by

$$R_0^2 = \frac{9\pi h^3 Y_e^2}{4Gm_u^2 m_e^2 c} \quad (18)$$

then the first differential equation is

$$\frac{dy}{dx} = -\frac{yz}{x^2 \gamma(y)} \quad (19)$$

2.1.3 Mass-radius relationship

Consider a thin shell of thickness dr at a radius r , the mass of this shell, dm , is given by

$$\frac{dm}{dr} = 4\pi r^2 \rho \quad (20)$$

Therefore, using the substitutions from equation 14 and the definition of M_0 , equation 16, the last differential equation becomes

$$\frac{dz}{dx} = 4\pi x^2 y \frac{R_0^3 \rho_0}{M_0} = 3x^2 y \quad (21)$$

2.2 Solving the partial differential equations

The two partial differential equations, equations 19 and 21, can be solved simultaneously using the Runge-Kutta method. The Runge-Kutta algorithm is a numerical method. It works by starting at an initial value and iteratively calculating subsequent values using the gradient calculated from the partial differential equations.

The implementation of Runge-Kutta used was `solve_ivp` by SciPy (SciPy 2022a). The `solve_ivp` method requires defining the integration range for x and the initial values for y and z .

The constants R_0 , ρ_0 and M_0 are used to define x , y and z ; therefore, these values will be defined first. The three constants depend on well known constants with the exception of Y_e . As Y_e is given by the reciprocal of equation 1, then for standard white dwarf stars, $Y_e = \frac{1}{2}$, however, for an iron-core white dwarf, $Y_e \approx \frac{26}{55.85}$.

Therefore, for standard white dwarf stars, $R_0 = 9.60 \times 10^{-3} R_\odot$, $\rho_0 = 1.40 \times 10^6 \rho_\odot$ and $M_0 = 1.23 M_\odot$.

For an iron white dwarf star, this would change to $R_0 \approx 8.93 \times 10^{-3} R_\odot$, $\rho_0 \approx 1.50 \times 10^6 \rho_\odot$ and $M_0 \approx 1.07 M_\odot$.

2.2.1 Internal structure of a white dwarf

The internal structure of a white dwarf can be calculated by specifying the initial values for y and z , which correspond to the center of the white dwarf. As z corresponds to the mass, this value will be zero. However, as y corresponds to the density, it will be a maximum at the center of the star; therefore, the core density defines the properties of the white dwarf.

The value for y could be chosen based on a logical guess for the central density of a white such as using the numbers from [Leung & Nomoto \(2018\)](#); however, a more applicable range of values can be chosen if the full range of densities is known. The density range is calculated in section 2.2.2. Four core densities are then chosen to produce masses linearly distributed up to the Chandrasekhar mass. However, due to the radius tending towards zero as the mass goes towards the Chandrasekhar mass, an upper limit of $1.4 M_{\odot}$ was chosen as this will still give a good representation of high mass white dwarfs while also having a realistic radius and pressure. A lower limit of $0.12 M_{\odot}$ was also taken to compare an iron white dwarf of the same radius to a carbon-oxygen one.

The corresponding core densities for y were $2.78 \times 10^4 \rho_{\odot}$, $1.70 \times 10^6 \rho_{\odot}$, $1.79 \times 10^7 \rho_{\odot}$ and $4.11 \times 10^9 \rho_{\odot}$ for masses $m = 9.34 \times 10^{-2} M_{\odot}$, $m = 0.537 M_{\odot}$, $m = 0.963 M_{\odot}$ and $m = 1.40 M_{\odot}$, respectively.

Finally, as x is the integral range for the solve_ivp method, which corresponds to the radius of the white dwarf, scaled by R_0 , the upper limit would be expected to vary for different white dwarfs of different core densities. If the upper limit is too large, the calculation will fail.

Another problem is that solve_ivp will also fail if $x_{min} = 0 R_0$ or if it is too small; therefore, each star will have a unique lower limit.

For now, the values will be taken to be $8.93 \times 10^{-5} R_0$, $2.44 \times 10^{-5} R_0$, $1.17 \times 10^{-5} R_0$ and $2.10 \times 10^{-6} R_0$ for the lower limits, and $2.59 \times 10^{-2} R_0$, $1.28 \times 10^{-2} R_0$, $8.02 \times 10^{-3} R_0$ and $2.13 \times 10^{-3} R_0$ for the upper limits for the respective stellar masses. These values are calculated as seen in section 2.2.2.

Due to the continuous nature of the model and the assumption of no atmosphere, there is no clear point for the surface. A minimum density could be taken, which would classify the boundary between the internal structure and the atmosphere of the white dwarf. In a paper by [Rohrmann \(2001\)](#), they found that the density of the atmosphere of a white dwarf can reach magnitudes of 10 kg m^{-3} . However, this value for the atmospheric density was not taken into account. It is insignificant compared to the densities involved, so the impact on the total radius would be negligible. However, not properly accounting for the point of the surface will introduce some inaccuracies in the model.

2.2.2 Mass, density and radii properties of white dwarfs

The same method in section 2.2.1 can be used to calculate how the total mass, radius and core density vary between white dwarfs. However, a range of core densities can be simulated instead of manually picking four white dwarf stars with chosen core densities and x limits.

The maximum mass and radius will be taken as properties of a white dwarf with the defined core density. Each core density's total mass and radius values can be plotted to show the desired relationships.

The range of values for y will have to be chosen to represent the full range of possible white dwarf masses. A lower limit to the core density, y_{min} of $2.79 \times 10^4 \rho_{\odot}$ to a maximum core density, y_{max} , of $1.4 \times 10^{17} \rho_{\odot}$. The lower limit of y was chosen as it produced white dwarfs with masses as low as $0.0934 M_{\odot}$, which is below the

current known smallest white dwarf of mass $0.17 M_{\odot}$ as found in a paper by [Kilic et al. \(2007a\)](#). A follow-up paper by the same authors, ([Kilic et al. 2007b](#)), also suggest that the binary star orbiting the white dwarf has a mass around $0.1 M_{\odot}$ and they suggest this could also be a white dwarf; however, there is currently not enough evidence to confirm this. Therefore, the lower limit for y is suitable to represent the white dwarf population.

The upper limit, y_{max} , was chosen to produce densities of $1.40 \times 10^{17} \rho_{\odot}$, which surpasses the densities seen by [Leung & Nomoto \(2018\)](#) from particles originating from a white dwarf.

The values within this range will follow a logarithm distribution due to the significant differences in magnitudes.

Finally, the limits of integration for solve_ivp have to be defined. If the lower limit is too small or the upper limit is too high, then the integration will fail.

The lower limit of integration for solve_ivp, x_{min} was chosen to follow a logarithmic distribution in the range $9.60 \times 10^{-5} R_0$ for low core density white dwarfs, and $9.60 \times 10^{-9} R_0$ for the highest core density stars. A range of values was used instead of a fixed value due to higher core density white dwarfs having a smaller radius; therefore, the lower limit needs to be smaller to account for this.

For the upper limit, x_{max} , a simple logarithmic scale would not work for every white dwarf within the range due to the upper limit having a more significant impact on the properties of the star; therefore, a different method has to be used. Solving this problem involved taking advantage of the pass-fail condition of solve_ivp. If the upper limit for x is too large, then the algorithm would fail; therefore, x_{max} can be found by converging on a small value close to the point of the pass-fail value.

An initial value of $x_{max} = 2.78 \times 10^{-2} R_0$ was chosen as this is close to the upper limit for the lowest mass star. Then the initial guess for x_{max} was multiplied by a scalar with an initial value of 0.9. This scalar value converges to one after each iteration in half steps for a minimum of 10 iterations, and the result of solve_ivp is successful. A value of 10 was chosen as this balances processing time and the model's accuracy.

The range of values for x_{max} found by the model was $2.74 \times 10^{-2} R_0$ for low mass white dwarfs, and $8.23 \times 10^{-6} R_0$ for high mass white dwarfs.

2.2.3 Comparison with existing data

Finally, existing data collected from two surveys of white dwarfs can be compared with the iron-core and carbon-oxygen models to assess their validity.

The model will be compared with several measurements of the stellar mass and radius of different white dwarf stars. The majority of the measurements are from a paper by [Provencal et al. \(1998\)](#), however, Stein 2051 was taken from [Altamirano \(2022\)](#), the 1974 measurement of 40 Eri B from [Heintz \(1974\)](#), the 2017 measurement from [Bond et al. \(2017\)](#) and the 2002 measurement of Procyon B from [Provencal et al. \(2002\)](#).

Then, the model will be compared with some data taken from the Sloan Digital Sky Survey (SDSS) [Rebassa-Mansergas et al. \(2012\)](#). As the survey covered a much vaster range of white dwarfs, more data could be collected, and therefore, the data taken for this report could be more specific. There were 25 white dwarfs taken for SDSS and were partially chosen by random, with a bias towards data with low uncertainties and an even distribution of masses.

3 RESULTS

The results from the model can be broken up into three sections. The first is the relationship between mass and density over a range of radii for a singular white dwarf of a given core density value. The second is to compare a range of white dwarfs with different core density values and compare the relationship of mass and density against the radius. Finally, the model can be compared to data from white dwarfs of known mass and radius to identify the model's effectiveness and if there is enough evidence to suggest the existence of iron-core white dwarfs.

3.1 Structure of a white dwarf star

The relationship of density as a function of white dwarf radius can be seen in figure 1 for four different white dwarfs, with $\frac{A}{Z} = 2$, of masses $0.12 M_{\odot}$, $0.54 M_{\odot}$, $0.96 M_{\odot}$ and $1.40 M_{\odot}$, and four iron white dwarfs of the same radius. The fractional density is relative to the carbon-oxygen white dwarf.

As can be seen from the figure, lower mass white dwarfs have lower densities. For white dwarf a, it has a maximum density of $4.33 \times 10^4 \rho_{\odot}$, star b has $1.70 \times 10^6 \rho_{\odot}$, star c has $1.79 \times 10^7 \rho_{\odot}$ and star d has $4.11 \times 10^9 \rho_{\odot}$. Therefore, there are about five magnitudes of change in density for about one magnitude of change in mass.

However, the white dwarf radius has an inverse relationship to the total mass as the white dwarfs have radii $0.025 R_{\odot}$, $0.013 R_{\odot}$, 8.4×10^{-3} and 2.2×10^{-3} for white dwarfs a, b, c and d respectively.

All four white dwarfs over the range of masses show very similar density-radius profiles. At low radii, the density is at a maximum with only a small change in density for a slight increase in radius. However, as the radius increases, there is a dramatic decrease in density until it plateaus again for large radii.

The fractional radius where the density decreases by 10% is found at 17% for the lowest mass star, 15% and 12% for stars b and c, respectively, and 8% for the highest mass star. Likewise, at the other tail end, where the density has decreased to 10% occurs at 76% for star a, 72% for star b, 64% for star c and for star d; this drops to 44%.

When comparing the carbon-oxygen density-radius relationship to the iron-core white dwarf, it can be seen that both types show a very similar trend in radius; however, the magnitude in density differs. For white dwarfs of the same total radius, iron white dwarfs have a smaller density throughout the range of radii. For stars a and b, carbon-oxygen white dwarfs are 1.45 times denser, while for stars c and d, it is only 1.25 times as much. However, there is no clear trend for the differences in densities at higher radii.

When comparing the mass-radius profiles for each of the four white dwarfs, figure 2, it can be seen that the mass enclosed at a given radius increases as the radius increases. The mass-radius relationship follows a similar trend to the density profile with a rough s-shape, however, flipped horizontally.

At small radii, the enclosed mass is negligible; however, the enclosed mass rapidly increases during intermittent radii until it finally plateaus again for large radii.

The fractional radii where the mass enclosed decreases by 10% are found at 77%, 76%, 72% and 59% for stars a, b, c and d, respectively. Likewise, when the radius only encloses 10% of the mass, it occurs at fractional radii of 27%, 25%, 22% and 16% for stars a to d, respectively.

When comparing the iron-core white dwarfs to carbon-oxygen white dwarfs with the same radius, it can be seen that iron white dwarfs have a smaller mass throughout the whole radius range, with the most significant differences being at large radii. As the total mass

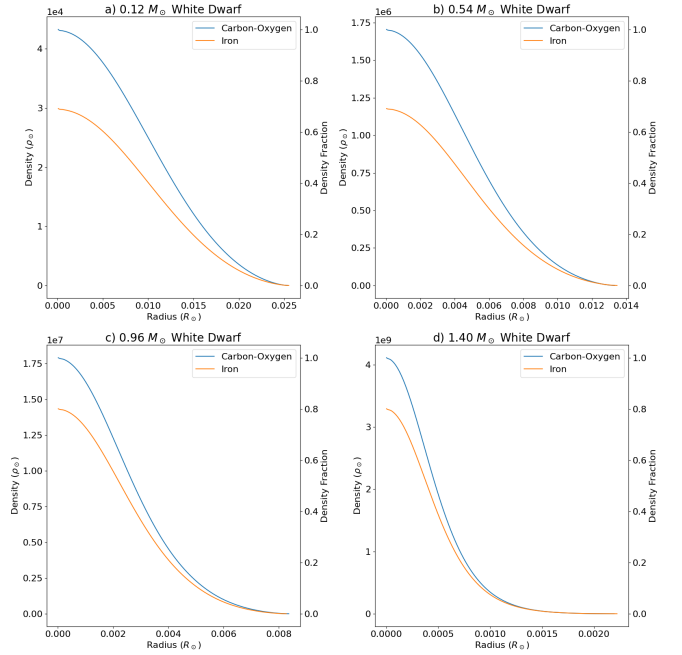


Figure 1. Density as a function of radius for four different carbon-oxygen white dwarf masses. The orange line shows an iron white dwarf of an equivalent radius but smaller mass. Plots a, b, c and d show the relationship for white dwarf masses of $0.12 M_{\odot}$, $0.54 M_{\odot}$, $0.96 M_{\odot}$ and $1.4 M_{\odot}$, respectively.

is given by the mass enclosed at the largest radius, the total masses between iron-core and carbon-oxygen white dwarfs can be compared. For low mass carbon-oxygen white dwarfs, star a, iron white dwarfs of the same radius have a mass that is 70% of the total mass. However, the difference in mass decreases as the radius decreases and the carbon-oxygen mass increases. For star b, the difference is 75%, then 82% for star c and 87% for the highest mass white dwarf.

However, at the smallest radii, the mass difference between the two types of white dwarfs is independent of the total mass. Iron-core white dwarfs are a constant 87% of the mass of the carbon-oxygen counterpart.

3.2 Mass, density and radii properties of white dwarfs

Figure 3 shows how the simulation of many white dwarfs with different core density starting conditions can produce a relationship showing how the total mass of a white dwarf varies with the total radius. It can be seen from the graph that, while the overall shape of each white dwarf may be similar when compared to other white dwarfs, the properties can dramatically vary. In the range of masses from $0.12 M_{\odot}$ to $1.4 M_{\odot}$, the high mass white dwarfs show the same distribution compressed over a much smaller radius range while also covering a much more extensive mass range. Therefore, high mass white dwarfs have a significantly higher gradient, whereas low mass white dwarfs have a shallow gradient.

The relationship between the physical properties of white dwarfs can be seen clearer in figure 4 as well as the comparison with iron-core white dwarfs. Due to the extensive ranges of density magnitudes, the y axis has been changed to a logarithmic scale.

The core density against radius shows a nearly linear relationship between $\log \rho$ and radius until around a core density of $10^{11} \rho_{\odot}$ where the plot asymptotes at $r = 0$. The gradient during the linear part of the model, the gradient can be estimated using curve_fit from

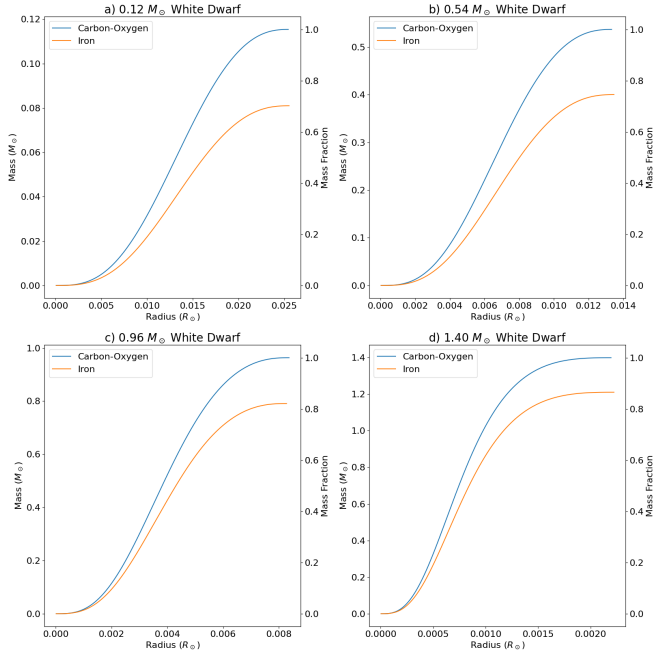


Figure 2. Enclosed mass as a function of the radius of a white dwarf for four different carbon-oxygen white dwarf masses. The orange line shows an iron white dwarf of an equivalent radius but smaller mass. Plots a, b, c and d show the relationship for white dwarf masses of $0.12 M_{\odot}$, $0.54 M_{\odot}$, $0.96 M_{\odot}$ and $1.4 M_{\odot}$, respectively.

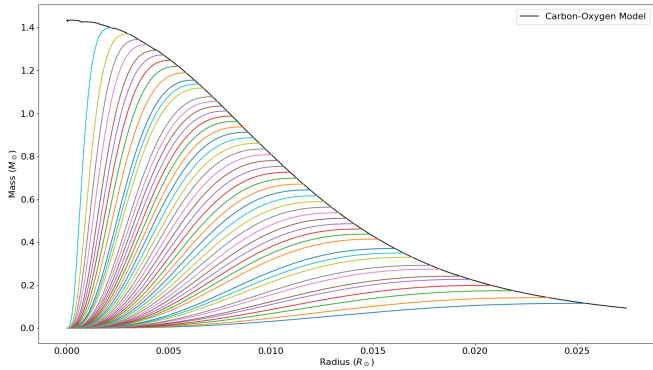


Figure 3. Contribution of several carbon-oxygen white dwarfs' enclosed mass-radius relationship to create the total mass-radius relationship.

SciPy (SciPy 2022b) with an estimated gradient of $-168.4 \pm 3.7 R_{\odot}^{-1}$; however, this is a crude averaged estimate. The same can be done for iron white dwarfs, which gives a gradient of -177.8 ± 3.8 .

When comparing iron white dwarfs with the standard type of white dwarfs, iron white dwarfs with the same radius will have a lower density than the carbon-oxygen counterpart. The carbon-oxygen white dwarfs are 1.45 times denser than the iron equivalent for large radii. A value of $0.005 R_{\odot}$ was chosen for smaller radii as this occurs before the asymptote at the origin. The difference has decreased to 1.25 times denser for carbon-oxygen white dwarfs.

For figure 4.b, this shows the mass-radius relationship for standard and iron-core white dwarfs.

The total mass as a function of radius shows a similar S-shaped curve as seen in section 3.1 with an asymptote at low radii to a max-

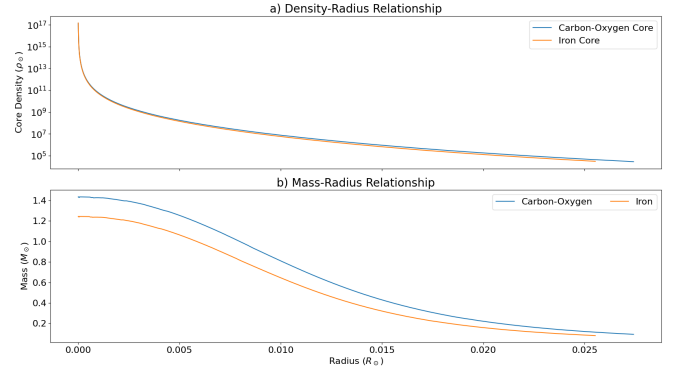


Figure 4. White dwarf core density-radius relationship (a) and stellar mass-radius relationship (b) for carbon-oxygen and iron-core white dwarfs. The density scale is logarithmic.

imum mass. The asymptotic mass for carbon-oxygen white dwarfs is $1.43 M_{\odot}$ while for iron white dwarfs, this value is only $1.24 M_{\odot}$. Therefore, carbon-oxygen white dwarfs can reach masses 1.15 times larger than iron white dwarf stars.

Over the whole radius range, carbon-oxygen white dwarfs always have a greater mass than iron white dwarfs. The difference in magnitude increases as the radius increases to 1.42 times more massive at a radius of $0.025 R_{\odot}$.

In section 3.1, it was found that between the $0.54 M_{\odot}$ and $0.96 M_{\odot}$ white dwarfs, the ratio of core densities between the carbon-oxygen and iron white dwarfs changed from a constant 1.45 to 1.25, which will now be investigated further. The sample size was increased to 100 white dwarfs to narrow down the radius to $1.11 \pm 0.01 \times 10^{-2} R_{\odot}$, the point where the change occurs.

3.3 Comparison with existing data

Figure 5 shows the same relationship as seen in section 3.2; however, data from several studies on white dwarfs have been added.

As can be seen from figure 5, the majority of the white dwarf stars are around $0.6 M_{\odot}$ with the highest mass white dwarf being Sirius B of $1.00 \pm 0.02 M_{\odot}$ and the lowest being 40 Eri B from 1974 with a mass of $0.43 \pm 0.02 M_{\odot}$.

The range of radii for the white dwarfs are from $8.4 \pm 0.2 \times 10^{-3} R_{\odot}$ for Sirius B, to $1.5 \pm 0.1 \times 10^{-3} R_{\odot}$ for W485A.

The data taken from SDSS can be seen in figure 6. The range of masses cover white dwarfs from $0.27 \pm 0.03 M_{\odot}$ to $1.46 \pm 0.05 M_{\odot}$. The range of radii are from $2.70 \pm 0.56 \times 10^{-3} R_{\odot}$ to $2.67 \pm 0.16 R_{\odot}$.

When compared to figure 5, the white dwarfs from SSDS tend to follow a much tighter trend and generally have a higher mass for a given radius. The averages of each data set can be compared using a weighted average, as seen by the purple cross. When compared with the carbon-oxygen white dwarf line, the weighted average of the SSDS data set lies just above this line, whereas, for the first group of white dwarfs, it lies between the carbon-oxygen and iron white dwarf lines. However, this weighted average method is a crude way of comparing results due to the non-linear nature of the data; however, due to the roughly even distribution, it should still provide valuable insight.

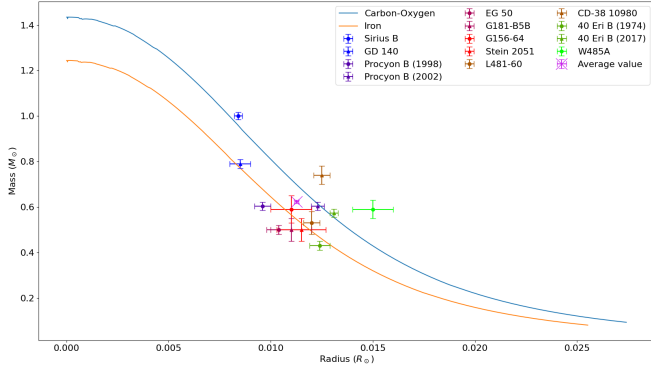


Figure 5. Stellar mass-radius relationship with data from several sources. Stein 2051, Eri B (1974), Eri B (2017) and Procyon B (2002) are from Altamirano (2022), Heintz (1974), Bond et al. (2017) and Provencal et al. (2002), respectively. The remaining stars are from Provencal et al. (1998). The purple cross represented the weighted average of all data points.

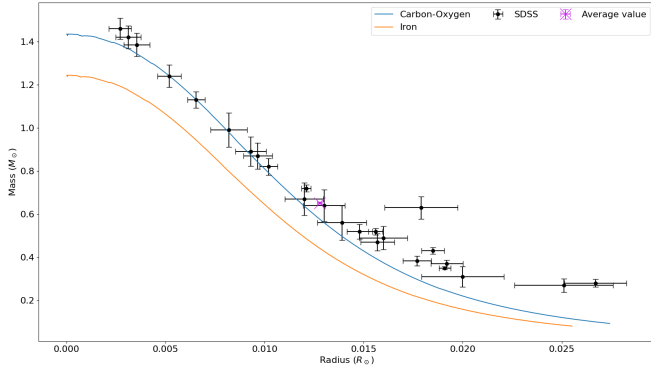


Figure 6. Stellar mass-radius relationship with data from SDSS Rebassa-Mansergas et al. (2012). The purple cross represented the weighted average of all data points.

4 DISCUSSION

The following sections will discuss the results found in section 3. The main inaccuracies that affect all the results would be the assumptions mentioned in section 2, as well as some additional ones mentioned here.

One inaccuracy will come from the problem of trying to model the surface of the white dwarf. This problem is challenging as the model does not account for a surface boundary condition; therefore, it is difficult to decide where the surface should start. It can be seen in figure 1 that each mass type has a different cut off point. This cut-off point varies in density and the corresponding radii. Therefore, this would affect the total radius predicted by the model.

Another potential source of uncertainty can come from the assumption that the stars are modelled as zero-temperature stars; therefore, the only form of pressure comes from electron degeneracy pressure. However, in a paper by Sahu et al. (2017) and Pani et al. (1999), they show that different temperatures have different mass-radius relationships, with higher temperatures having a larger mass for the same radius.

4.1 Structure of a white dwarf star

As seen in section 3.1, as mass increases, the core density also increases. This relationship is due to the gravitational force equation, which depends upon mass, which would create a more considerable pressure acting on the core. This pressure will compress the material into a smaller volume, increasing the density throughout the white dwarf, including the core, and reducing the overall radius. The radius reduction can be seen by comparing the maximum radius calculated by `sovlv_1vp` with white dwarfs with larger masses having a smaller radius.

However, when comparing the shapes of the distributions to the total radius, due to the problems mentioned above with quantifying the maximum radius, the values found for the 10% and 90% density radius would need a more accurate model to identify if these values still hold up. However, suppose these values are accurate. They show a clear trend that as the total mass increases, the high-density regions shift closer to the core with a more prominent low-density envelope.

To now compare the results with the iron white dwarf model, it can be seen that iron white dwarfs of the same radius have lower core densities. However, due to the fewer electrons per nucleon of iron, it would be expected that iron-core white dwarfs have a greater density. This problem can be solved by looking at the mass-radius relationship and seeing that more massive iron white dwarfs are shifted to lower radii; therefore, carbon-oxygen white dwarfs are more massive for the same radius.

However, a rather intriguing result was the difference between the core density of carbon-oxygen and iron white dwarfs. For low mass white dwarfs, this difference was around 1.45 times; however, for high mass white dwarfs, this changed to 1.25 times. The point of change occurs around $1.11 \pm 0.01 \times 10^{-2} R_{\odot}$ as seen in section 3.2. This radius lines up with the point of inflection of the carbon-oxygen white dwarf mass-radius relationship at around $0.71 \pm 0.01 M_{\odot}$. As the change in ratios occurs after a point of inflection, it would suggest that the iron white dwarf mass-radius relationship is trailing behind the carbon-oxygen one. Therefore, when the carbon-oxygen white dwarf trend reflects, a new difference between the two is induced. Due to the close relationship between radius, density and mass, the change in the mass-radius relationship can be reflected in the density-radius relationship creating the observed effect.

For the mass-radius relationship of a white dwarf, similar comments can be made about where the radius encloses 10% and 90% of mass. However, if this is assumed accurate, then it can be seen that for higher mass stars, there is a faster build-up of mass at lower radii, and therefore, the majority of the mass of the white dwarf is enclosed at smaller radii. This relationship agrees with what was found for the density relationship, as more dense regions would have more mass for a given radius range.

It was found in section 3.1 that, when comparing carbon-oxygen and iron white dwarfs, as the total mass increases, the ratio of masses of an equivalent radius iron white dwarf increases. Therefore, there is a more negligible difference between high mass white dwarfs. From the Chandrasekhar mass limit, it would be expected that the maximum mass of an iron white dwarf can only reach 87% of a carbon-oxygen white dwarf. As the difference in figure 2.d shows a difference of 87% mass, then they are already showing the limits of the Chandrasekhar mass.

4.2 Mass, density, and radii properties of white dwarfs

This section uses results found in section 2.2.2.

When comparing the core densities between carbon-oxygen and

iron white dwarf stars, it can be seen that they roughly follow a linear trend between $\log \rho_{\odot}$ and radius. However, this relationship is not exact, as, throughout this region, there is a slight positive curvature. However, the crude approximation of the linear approach can show that iron-core white dwarfs have a steeper gradient than the standard types of white dwarfs. The steeper gradient means that the core density is more sensitive to radius for iron white dwarfs.

It can be seen that the asymptote at $r = 0$ R_{\odot} will result in a singularity as the density goes to infinity due to the mass tending towards a constant value. This singularity is where Chandrasekhar's mass comes in, as the density will reach a point where electron capture will be triggered. When electron capture is triggered, there will be a sudden loss of electron degeneracy pressure in the core, resulting in a rapid runaway electron capture and fusion process. This process is what causes type Ia supernovae.

The asymptotic value is the Chandrasekhar mass, and as seen in section 1, which should be $1.44 M_{\odot}$ for $\frac{A}{Z} = 2$ for standard white dwarfs, and $1.25 M_{\odot}$ for iron white dwarfs. The values obtained from the simulated data is $1.43 M_{\odot}$ for $\frac{A}{Z} = 2$, and $1.24 M_{\odot}$ for iron white dwarfs. Both results have negligible differences in agreement between the asymptotic values from the model. Compared to the theoretical values, both results only have a difference of $0.01 M_{\odot}$. Therefore, the negligible difference suggests that the model has good agreement with the theoretical maximum of white dwarfs. However, the inaccuracies and assumptions mentioned earlier could explain the slight difference in results.

4.3 Comparison with existing data

This section will use the results noted in section 3.3.

The first data comparison is with [Provencal et al. \(1998\)](#) data set with a few additional white dwarfs.

From this data, it can be seen that it generally agrees with the model; however, many of the white dwarfs have lower masses than expected, falling closer to the iron line. In particular, the three stars mentioned in section 1 can be seen close to, or below, the iron line. These stars are 40 Eri B (1974), Procyon B (1998), GD 140 and EG 50. These four stars all show several deviations of uncertainty from the carbon-oxygen line, suggesting that these stars are likely to be iron white dwarfs.

However, as seen in the two follow-up measurements of 40 Eri B (2017) and Procyon (2002), even though they had low uncertainties in the original measurement, the new measurements have dramatically changed this value. Both of these stars now lie on the carbon-oxygen line confirming that these stars are likely to follow the standard model of white dwarfs.

The removal of previous candidates due to new data suggests that even though some of the white dwarfs measured have lower masses than expected and low uncertainties, their actual value can dramatically vary when new measurements update these values. Therefore, even though there have not been any new measurements for GD 140 and EG 50, that does not confirm that these give evidence for iron white dwarfs as they could follow similar paths to what Procyon B and 40 Eri B experienced. However, as these white dwarfs do not have updated values, it also means that iron white dwarfs cannot be ruled out as a potential form of a remnant star.

If the model is now compared with the SSDS data set, there is a dramatic difference between the data in figures 6 and 5. All white dwarfs taken from the SDSS data set now fall on the carbon-oxygen line or above it. Therefore, two conclusions can be made from this observation. The first is that iron white dwarfs are either incredibly unlikely, and a generalist survey like SDSS will have a bias towards

the average rather than a more targeted search from [Provencal et al. \(1998\)](#). Alternatively, iron white dwarfs cannot be produced naturally, as there is little evidence to suggest the existence of iron white dwarfs, and previous measurements suffer from inaccuracies of old instruments and techniques.

The data from SDSS closely follows the model for intermediate to high mass white dwarfs in the range from around $0.6 M_{\odot}$ to $1.3 M_{\odot}$, however, for very high mass white dwarfs or low mass white dwarfs, there is a discrepancy between the model and the data.

For high mass white dwarfs, the model tends to underpredict the mass for a given radius; however, some of the data from SDSS measured white dwarfs with masses above the Chandrasekhar mass limit. These super-massive white dwarfs could be due to inaccuracies in the measurements or phenomena that allow for masses that surpass the Chandrasekhar mass not accounted for in the model. Potential examples are spinning white dwarfs, temperature and highly magnetised white dwarfs.

For low mass white dwarfs, it can also be seen that the model is underpredicting the mass of a white dwarf for a given radius. The larger values than expected could be due to the significant uncertainties involved with low mass white dwarfs; however, the data from masses below $0.6 M_{\odot}$ shows a separate trend curving to values higher than predicted by the model. Some possible explanations are that unaccounted phenomena are responsible for white dwarfs with lower densities, or atmospheres of white dwarfs could be affecting the measurement for the radius, therefore, predicting a larger radius for the same mass.

5 CONCLUSIONS

This paper aimed to model the internal structure of white dwarf stars. As the equations of state mainly depend upon constants, there is only one free parameter. This parameter is determined by the number of electrons per nucleon and gives rise to different types of white dwarf stars. From the evolution of main-sequence stars to white dwarfs, there are three main types of white dwarfs, helium, carbon-oxygen and neon-magnesium. However, there is also a theorised iron white dwarf. As helium, carbon, oxygen, neon and magnesium all have the same ratio of electrons per nucleon, these will all follow the same equations of state; however, iron-core white dwarfs will have a different relationship.

It was found that iron white dwarfs are smaller, more dense objects; however, they follow the same trend as the main types of white dwarfs. Both types will asymptote at a specific mass as the radius tends towards zero. Theoretical models predict this, and the mass is called the Chandrasekhar mass. The values predicted by the model are $1.43 M_{\odot}$ for the main types and $1.24 M_{\odot}$ for iron-core. The values from the model are within $0.01 M_{\odot}$ of the theoretical value; therefore, this suggests that the model is good at predicting the nature of high mass remnant stars.

The model can then be compared with data collected from primarily two data sets. The first was from [Provencal et al. \(1998\)](#), and the second was from a more recent survey by SDSS, ([Rebassa-Mansergas et al. 2012](#)).

In the first survey, the data generally agreed with the model; however, the white dwarfs had lower masses than predicted. This mass discrepancy would suggest that they are potential iron white dwarf candidates. However, follow up reports updated some of the masses of the white dwarfs, placing them in line with the expectation of carbon-oxygen white dwarfs. However, several data points remain as

potential iron-core white dwarfs. Therefore, the results from this data set are inconclusive on the existence of iron white dwarfs.

The more recent survey by SDSS provided a large data set of data points; however, there were no iron-core white dwarf candidates from the data sampled. In contrast, some of the white dwarfs had masses larger than predicted by the carbon-oxygen model, providing counter-evidence for the existence of iron-core white dwarfs.

This report has not found any conclusive evidence for iron-core white dwarfs, and more recent data suggest the counter-argument that iron white dwarfs are not physically possible. However, the model used in this paper suffers from several assumptions resulting in slight deviations in the data. Some of the assumptions are not accounting for the spin of a white dwarf, the temperature and not correctly handling the surface limit of the white dwarf.

REFERENCES

- Altamirano D., 2022, Structure of White Dwarf Stars
 Bond H. E., Bergeron P., Bédard A., 2017, *The Astrophysical Journal*, 848, 16
 Chabrier G., Baraffe I., 1997, arXiv preprint astro-ph/9704118
 Chandrasekhar S., 1984, *Science*, 226, 497
 Dormand J., Prince P., 1978, *Celestial Mechanics*, 18, 223
 Dormand J. R., Prince P. J., 1980, *Journal of computational and applied mathematics*, 6, 19
 Figueroa A., Jackiewicz Z., Löhner R., 2021, *International Journal for Numerical Methods in Fluids*, 93, 429
 Heger A., Fryer C. L., Woosley S. E., Langer N., Hartmann D. H., 2003, *The Astrophysical Journal*, 591, 288
 Heintz W., 1974, *The Astronomical Journal*, 79, 819
 Isern J., Canal R., Labay J., 1991, *The Astrophysical Journal*, 372, L83
 Ishikawa A., Michels D. L., Yaguchi T., 2018, *Japan Journal of Industrial and Applied Mathematics*, 35, 511
 Jordan G. C., Perets H. B., Fisher R. T., van Rossum D. R., 2012, *The Astrophysical Journal Letters*, 761, L23
 Kilic M., Prieto C. A., Brown W. R., Koester D., 2007a, *The Astrophysical Journal*, 660, 1451
 Kilic M., Brown W. R., Prieto C. A., Pinsonneault M., Kenyon S., 2007b, *The Astrophysical Journal*, 664, 1088
 Leung S.-C., Nomoto K., 2018, *The Astrophysical Journal*, 861, 143
 Panei J., Althaus L., Benvenuto O., 1999, arXiv preprint astro-ph/9909499
 Pols O., 2011, *Stellar Structure and Evolution*, Utrecht University Lecture Notes
 Provencal J. L., Shipman H., Høg E., Thejll P., 1998, *The Astrophysical Journal*, 494, 759
 Provencal J., Shipman H., Koester D., Wesemael F., Bergeron P., 2002, *The Astrophysical Journal*, 568, 324
 Rebassa-Mansergas A., Nebot Gómez-Morán A., Schreiber M. R., Gänsicke B. T., Schwöpe A., Gallardo J., Koester D., 2012, *MNRAS*, 419, 806
 Rohrmann R., 2001, *Monthly Notices of the Royal Astronomical Society*, 323, 699
 Sahu K. C., et al., 2017, *Science*, 356, 1046
 SciPy 2022a, *scipy.integrate.solve_ivp*, https://docs.scipy.org/doc/scipy/reference/generated/scipy.integrate.solve_ivp.html
 SciPy 2022b, *scipy.optimize.curve_fit*, https://docs.scipy.org/doc/scipy/reference/generated/scipy.optimize.curve_fit.html
 Simos T., 2000, *Computational Materials Science*, 18, 315
 Tracogna S., Welfert B., 2000, *BIT Numerical Mathematics*, 40, 775
 Wei W., Dongsheng L., Chun L., 2013, in *2013 International Conference on Virtual Reality and Visualization*, pp 191–198
 Wikipedia 2022, Runge-Kutta methods, https://en.wikipedia.org/wiki/Runge%E2%80%93Kutta_methods#cite_note-notation-4
 Zhu M., Chang B., Fu C., 2018, arXiv preprint arXiv:1802.08831

APPENDIX A: RUNGE-KUTTA METHOD

The Runge-Kutta method is an iterative numerical algorithm that simultaneously solves multiple partial differential equations.

The general formula for all types of Runge-Kutta methods was given in a paper by Dormand & Prince (1980). There are several versions with different levels of accuracy. The different versions are labelled by RKN, where N is some integer and refers to the number of trial points to calculate the next step in the problem.

While the paper covers the different levels of the Runge-Kutta method, this paper will only discuss RK4 and briefly RK2, as these are the only relevant ones for this paper.

The method starts from an initial point and, given the differential equations, the gradient of that point and several small steps in the positive x-direction. This gradient can be used to estimate the coordinate of the next step, with the new point being the average of the estimates.

For variables x and y where $y = y(x)$, and $y' = f(x, y)$, and initial values x_n and y_n , the following point, y_{n+1} for a small step in the x-direction, h , can be found using the RK4 method (Wikipedia 2022),

$$x_{n+1} = x_n + h, \quad y_{n+1} = y_n + \frac{h}{6} (k_1 + 2k_2 + 2k_3 + k_4) \quad (\text{A1})$$

where

$$\begin{aligned} k_1 &= f(x_n, y_n), \\ k_2 &= f\left(x_n + \frac{h}{2}, y_n + \frac{hk_1}{2}\right), \\ k_3 &= f\left(x_n + \frac{h}{2}, y_n + \frac{hk_2}{2}\right), \\ k_4 &= f(x_n + h, y_n + hk_3), \end{aligned} \quad (\text{A2})$$

As can be seen from equation A1, more weight is given to gradients k_2 and k_3 as these are the mid points between x_n and x_{n+1} . The gradients k_2 to k_4 each use the previous gradient to find the point where the new gradient will be calculated.

The RK2 method is similar to the RK4 method; however, only two gradients are calculated, one at x_n and one at $x_n + \frac{h}{2}$.

As $h \rightarrow 0$, the error will vanish, similar to the same limit in integration or differentiation. The error will also decrease as the order of the method is increased. RK4 will have a smaller error than RK2 as there are more estimates from gradients for the following data point. Therefore, the error on the method is given by $O(h^{N+1})$ for one iteration, or a cumulative error of $O(h^N)$.

APPENDIX B: SCIPY SOLVE_IVP

solve_ivp, (SciPy 2022a) is an implementation of the Runge-Kutta method by SciPy for the programming language Python.

solve_ivp by default uses RK4, and this was used within this paper. This paper uses four arguments from the function.

The first is the function to be solved. This function has to be set up to simultaneously solve all partial differential equations. It will take in the current x value and the values for the other parameters in the equations. In this paper, the additional parameters would be y and z . The function will then return the differentials $\frac{dy}{dx}$ and $\frac{dz}{dx}$. The functions used in this paper can be found in section 2.1.

The following argument is *t_span*. This argument is the lower and upper limit of x that the function will try to integrate over. The

values used in this paper and the explanations for them can be found in section 2.2.2.

The third argument is the initial values for the parameters, y_0 . In this paper, it would correspond to the initial values for y and z at the center of the white dwarf. The value for z would be zero as this corresponds to zero mass enclosed at a zero radius. For the y parameter, this is discussed in section 2.2.2.

Finally, the last argument is t_{eval} , which is the number of evaluations at given x values to be saved. In this paper, a linear spacing of 1,000 values between the limits of integration was used.

APPENDIX C: USES IN PHYSICS

Due to the frequent appearance of partial differential equations in nature and the difficulty of solving them analytically, many numerical methods are developed to solve these problems. One numerical method is the Runge-Kutta method, as mentioned in appendix A and some possible applications for this method will be mentioned in this section.

An application for the Runge-Kutta method is in quantum mechanics to solve the Schrödinger equation. In a paper by Simos (2000), they explored the use of the Runge-Kutta method to solve Schrödinger's equation to problems with periodic or oscillating solutions. Several methods using the Runge-Kutta method were developed to try and efficiently solve this problem. These were exponential and trigonometric fittings for RK4 and RK2.

The paper is attempting to solve the one dimensional or radial Schrödinger equation which takes the form.

$$y''(x) + f(x)y(x) = 0 \quad (\text{C1})$$

where

$$f(x) = E - \frac{l(l+1)}{x^2} - V(x) \quad (\text{C2})$$

where E is the energy of the particle, $\frac{l(l+1)}{x^2}$ is the centrifugal potential and $V(x)$ is the potential. The potential terms have to tend towards zero as $x \rightarrow \infty$.

By taking advantage of the periodic differential properties of exponential and trigonometric equations, the paper found that this new method to solve periodic or solutions that oscillate was more efficient than current methods used in literature.

In a paper by Dormand & Prince (1978), they investigated the use of the Runge-Kutta method in orbital dynamics by incorporating efficiency improvements. The paper's main aim was to reduce the truncation error, the error per iteration, by managing the step size to minimise the truncation error without increasing the higher-order errors.

The improvements to the Runge-Kutta method were tested on a two-body problem and compared with alternative methods. The paper found that the lower order methods generally performed reasonably well with minor global errors for a limited number of iterations. However, the paper suggested that in applications where the initial conditions are less well defined, the higher-order terms would be more suited, and applications with many iterations are required.

While this paper only compared the methods in a two-body problem, the algorithms used are scalable to N-body problems.

In a different application, Figueroa et al. (2021) investigated the use of Runge-Kutta methods in fluid dynamics. Fluid dynamics have always posed a challenge and typically require high computational

costs. The paper aimed to reduce the time wasted in computer core communication, dominating the total simulation run time. The paper achieved this by implementing a two-step Runge-Kutta method. A two-step method uses two equations instead of equation A1. These equations can be seen below (Tracogna & Welfert 2000).

$$\begin{aligned} y_{n+1} &= \eta y_{n-1} + (1 - \eta)y_n + h \sum_{i=1}^s \left(v_i f(Y_i^{(n-1)}) + w_i f(Y_i^{(n)}) \right) \\ Y_i^{(n)} &= u_i y_{n-1} + (1 - u_i)y_n + h \sum_{j=1}^s \left(a_{ij} f(Y_j^{(n-1)}) + b_{ij} f(Y_j^{(n)}) \right) \end{aligned} \quad (\text{C3})$$

where $\eta, u_i, v_i, w_i, a_{ij}$ and b_{ij} are numbers given to the Runge-Kutta method of order s . The multi-step method tries to make future predictions to improve the accuracy of finding the next step, therefore, y_n is an approximation for $y(x_n)$ and $Y_i^{(n)}$ is an approximation to $y(x_n + c_i h)$. However, these extra approximations create more initial values that need to be known before running the model. If these values are not well known, it could add more uncertainty than it reduces. The additional parameters that need to be known for the two-step method are $Y_i^{(0)}$ as an approximation for $y(x_0 + c_i h)$ and y_1 as an approximation for $y(x_1)$.

Therefore, the paper accessed two scenarios for the method used in fluid dynamics. The first was a 2D cylinder experiment where the inflow and outflow characteristics were measured. The second was a 3D vortex that simulates how an initial flow condition results in a turbulent state through isotropic decay.

The paper found that the two-step Runge-Kutta method reduced the computation time by 25% over traditional methods without reducing the accuracy.

APPENDIX D: USES OUTSIDE OF PHYSICS

Outside of physics, the Runge-Kutta algorithm also has several uses, some of which are listed below.

The first is found in flight simulation programs as researched by a paper from Wei et al. (2013). The paper aimed to create realistic flight dynamics for flight training simulations. Flight simulators have to model different equations in real-time accurately. The paper aimed to solve two differential equations. The first is the center of motion for a rigid body, which describes the plane's velocity, engine thrust, and force. The second differential equation models the rotation of the center of mass of a rigid body; this is defined by the moment of inertia, the angular velocity and the roll moment. The paper found that the RK4 method simulated the dynamics in real-time, meeting the 60 frames per second target.

Another application is in machine learning, where a paper by Zhu et al. (2018) investigated the use of the Runge-Kutta method in convolutional neural networks (CNN) in machine learning.

Machine learning aims to design a network of functions with weights that can take an input and produce an output. The model's output is assessed, and a loss function is calculated. Based on the output of the loss function will determine how the weights for each function are updated. This process is repeated many times until the network achieves the desired accuracy. The input data is typically images passed into convolutional layers for a CNN. These layers work by sliding a matrix of weights over the input image to produce a new feature map. This process can be repeated several times with additional layer types, such as pooling layers, until the final feature map

is passed through a fully connected layer and an output is produced. The weights for each convolutional matrix can then be adjusted based on the loss function.

One type of CNN is a residual network. A residual network works by adding skip connections between layers so that, if the model deems it necessary, it can skip sections of the network. Skip connections allow for the creation of much deeper networks. The skip connection process can be considered a forward Euler method, equivalent to a first-order Runge-Kutta method. However, the paper aims to investigate the use of higher orders of Runge-Kutta methods to try and improve the accuracy of the network.

The paper assumes that CNNs can be modelled as time functions with each group of layers representing a different step in time or period, and time-dependent differential equations can model it. The partial differential equation aims to try and predict the output of each step. There are three types of layers for Runge-Kutta networks. The first is the preprocessor which takes the input data and applies the operator. The next type is multi-periods formed from multiple periods, each modelled by a time-dependent differential equation. Finally, the last type is the postprocessor, which takes the output from the last period or from multiple periods and passes this into a classifier.

The coefficients in each Runge-Kutta equation can be learned via training, with the relationship between coefficients having a more significant impact on the model's performance than the individual values. The step size is also learned by training; however, the number of steps is predefined.

The paper tested the Runge-Kutta neural network on several image classification data sets and found that the network surpassed state-of-the-art networks on small data sets while achieving equivalent performance on larger data sets.

Finally, in a paper by [Ishikawa et al. \(2018\)](#), they investigated the use of the Runge-Kutta method in the creation of musical sounds.

Musical sounds of different instruments can be represented by differential equations that model the physics of the instrument. One example is the oscillations of piano strings and the dynamics of the hammer. Several instruments share similar formats of differential equations; therefore, this method can be applied to various virtual instruments.

The paper's goal was to replicate realistic sounds of instruments so that video productions can easily create background sounds and music, or for cheaper and more diverse entry into learning instruments as one instrument could be used to replicate a variety of different ones.

Current synthetic techniques suffer from the difficulty of simulating the instrument's components, such as the interaction of hammers between the piano's strings and the interactions of the strings with the body. The aim is to use differential equations based on the instrument's physics to replicate the sounds that the instrument makes.

However, to accurately represent the sound produced, thousands of sound packets have to be simulated, which can cause numerical methods to fail due to the instability of multiple iterations. One way to get around this problem is to model the system's energy, which generally dominates the solution and is much more stable for long calculations. Therefore, the paper aims to create tools to automatically derive equations that preserve a significant property of the equations, such as the energy.

The paper managed to create a tool that could accurately produce sound waves over significant periods; however, in the current version, it lacked focus on spatial accuracy; therefore, this is an area for future work.

This paper has been typeset from a \LaTeX file prepared by the author.